

國立臺灣大學 理學院物理學研究所

碩士學位論文

Graduate Institute of Physics

College of Science

National Taiwan University

Master Thesis

在KOTO實驗中尋找無質量暗光子： $K_L^0 \rightarrow \gamma\bar{\gamma}$

Search for a massless dark photon in $K_L^0 \rightarrow \gamma\bar{\gamma}$ at the
KOTO Experiment

吳桐

Tong Wu

指導教授：熊怡 教授

Advisor: Yee Bob Hsiung, Ph.D.

中華民國113年8月

August 2024

NATIONAL TAIWAN UNIVERSITY

MASTER THESIS

**Search for a massless dark photon in
 $K_L^0 \rightarrow \gamma\bar{\gamma}$ at the KOTO Experiment**

Author:

Tong Wu

Supervisor:

Dr. Yee Bob HSIUNG

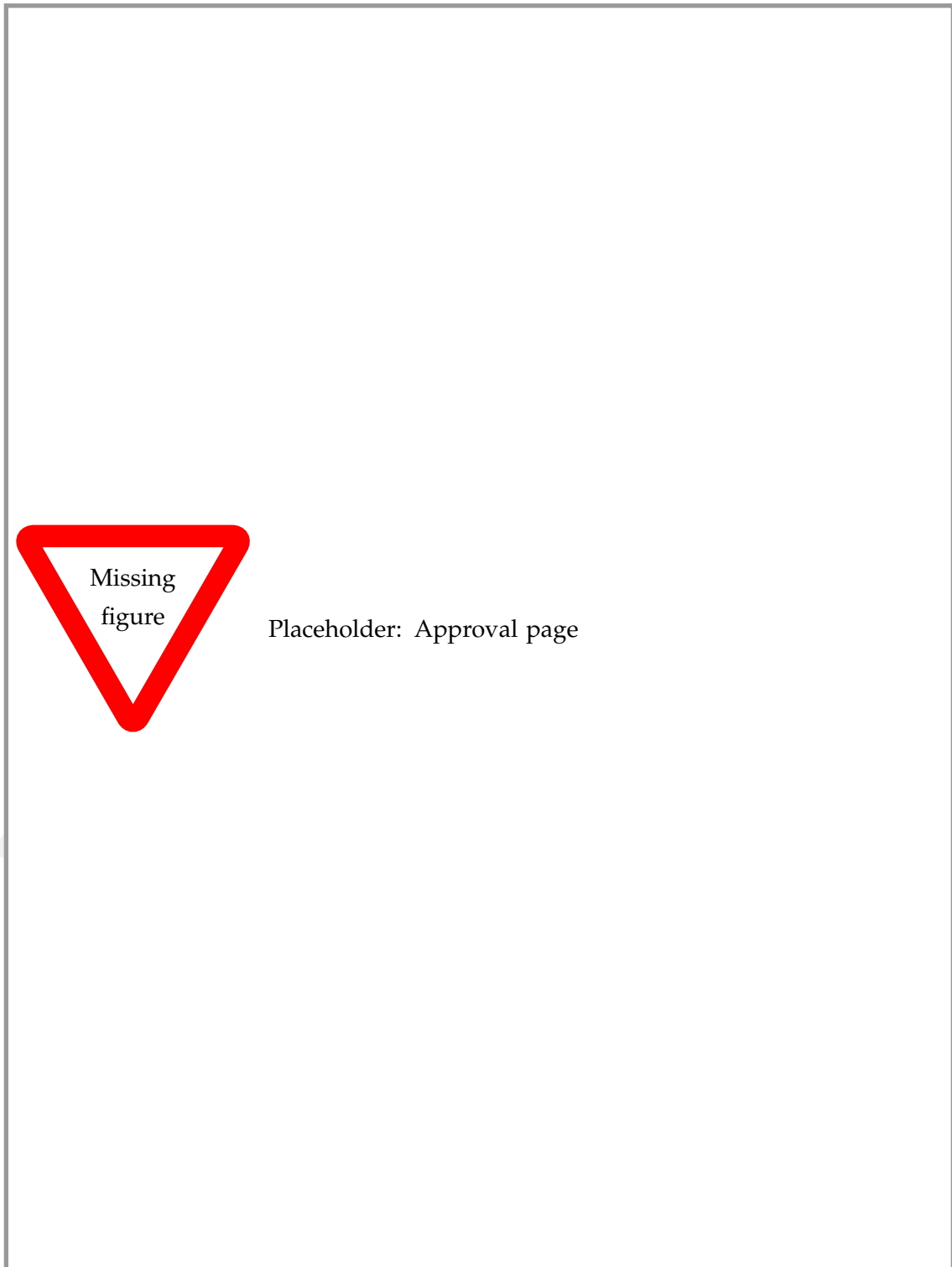


June 13, 2024

© 2024, by Tong Wu
tong@hep1.phys.ntu.edu.tw



ALL RIGHTS RESERVED



Acknowledgements

Thanks all

DRAFT

中文摘要

一二三

三二一

關鍵詞：暗光子、新物理。

Abstract

This thesis presents the search for the massless dark photon ($\bar{\gamma}$) in the $K_L^0 \rightarrow \gamma\bar{\gamma}$ decay at the J-PARC KOTO experiment, based on the special data collected in 2020.

Distinguished from the massive dark photon, the massless one does not directly mix with the ordinary photon but could interact with Standard Model (SM) particles through direct coupling to quarks. Some theoretical models propose that the branching ratio (\mathcal{BR}) of the $K_L^0 \rightarrow \gamma\bar{\gamma}$ decay could reach up to $\mathcal{O}(10^{-3})$.

The number of K_L^0 decays that had been collected in the special run is estimated to be $(1.29 \pm 0.02_{stat.}) \times 10^{10}$. The single event sensitivity is calculated to be $(2.91 \pm 0.02_{stat.}) \times 10^{-8}$. The total background level prediction is $(12.65 \pm 4.61_{stat.})$ with the agreement from the side-band region. We uncovered the blind region and observed 13 events. The Feldman-Cousins method is used to calculate the upper limit of the $K_L^0 \rightarrow \gamma\bar{\gamma}$ branching ratio to be $< 2.15 \times 10^{-7}$ (90%C.L.).

Keywords: Dark Photon, beyond Standard Model.

Contents

Approval	i
Acknowledgements	iii
中文摘要	v
Abstract	vii
Contents	ix
List of Figures	xi
List of Tables	xiii
1 Introduction	1
1.1 Motivation	1
1.2 Dark Photon	1
2 KOTO Experiment	3
2.1 Introduction	3
2.2 $K_L \rightarrow \pi^0 \nu \bar{\nu}$	3
2.3 Beam Line	3
2.4 Detectors	3
2.4.1 CsI	3
2.4.2 Barrel Veto	6
2.4.3 CV	6
2.4.4 Other Veto	6
2.5 Data Acquisition System	6
2.6 Data Taking	6
2.7 Trigger	6
2.8 Basic Strategy of the Single Cluster Study	6
2.8.1 Signal Identification	6
2.8.2 Major Background Sources	6
3 Event Reconstruction	9
3.1 Cluster Finding	9
3.2 Veto Hit Reconstruction	9
3.3 MPPC calibration	9
3.3.1 Cosmic Ray analysis	9
3.3.2 T0 correction	9

3.3.3 $K_L^0 \rightarrow 3\pi^0$ correction	9
4 K_L^0 Yield Estimation	11
4.1 Event Selections	11
4.2 Yield Estimation	11
5 Monte Carlo Simulation	13
5.1 GEANT4	13
5.2 Accidental Overlay	13
5.3 Beamline simulation	13
5.4 Other Simulations	13
5.4.1 NCC background	13
5.4.2 Halo Kaon	13
5.4.3 Charge Kaon	13
6 Analysis of $K_L \rightarrow \gamma\bar{\gamma}$	15
6.1 Event Selection	16
6.1.1 Trigger Selection	16
6.1.2 Kinematic Cuts	18
6.1.3 Veto Cuts	20
6.2 Background Suppression	20
6.2.1 K_L Decay Background	20
6.2.2 Hadronic Background	23
6.2.3 Low Radius Event background	26
6.3 Single Event Sensitivity	27
6.4 Background Level Estimation	27
6.5 Unblind and Results	27
6.6 Massive Dark Photon Search	27
7 Conclusion and Discussion	29
7.1 blah	29
Bibliography	31

List of Figures

2.1	The entire view of J-PARC. [2]	4
2.2	Beamline layout	4
2.3	CsI layout	5
6.1	Distribution of cluster timing after relative timing correction. The dot is from real physics data, and the filled histogram is the MC simulation. The red arrow is the cut-off region.	17
6.2	Distribution of total energy from Monte Carlo simulation. The histogram area is normalized to 1. The red arrow is the cut-off region.	18
6.3	An upstream view of the CsI calorimeter. The red region is the outermost boundary, while the blue region is the innermost boundary.	19
6.4	Temporary plots of FBAR and NCC	21
6.5	The schematic geometry diagram of the mechanism of the upstream decay background.	22
6.6	Todo-Fig: Change A B region in different color	
6.7	$E_\gamma - R_{XY}$ distributions of scattered $K_L^0 \rightarrow 2\gamma$ decays with various cut. The red frame indicates the signal region. The red number indicates the background level in each region.	22
6.8	Present the upper limit at 90% confidence level.	
6.9	$E_\gamma - R_{XY}$ distributions of various background sources after applying all selection cuts. Left-hand side plots exclude the neutron cuts and the right-hand side plots include it. The red frame indicates the signal region. The red number indicates the background level in each region.	24
6.10	The architecture of CSD neural network training process.	25
6.10	Distribution of the likelihood ratio for hadronic cluster events (red) and photon cluster events (blue). The photon cluster events are obtained through the $K_L^0 \rightarrow 3\pi^0$ decay analysis of data. The neutron sample is obtained from neutron data.	26

6.11 Illustration of shower depth means. An MPPC is installed on the upstream side. The time difference between the photon arriving upstream and downstream ($\Delta T = T_{MPPC} - T_{PMT}$) is used to measure the depth of the reaction and distinguish between photon events (left) and neutron events (right).	27
6.12 Distribution of the ΔT for neutron events and photon events. The photon cluster events are obtained through the $K_L^0 \rightarrow 3\pi^0$ decay analysis of data. The neutron sample is obtained by scattering neutrons in the beam with an Al plate.	27
6.13 The R_{XY} distribution of the region 2. The red line and arrow indicated the cutoff region	28

List of Tables

2.1	Main K_L^0 decay background modes and their branching ratios	6
4.1	Branching ratio of K_L decays	11
6.1	Number of events predicted for each source inside the signal region	28

Todo list

Figure: Placeholder: Approval page	i
█ Todo-Fig: Change A B region in different color	xi
█ Present the upper limit at 90% confidence level	xi
█ Add CsI dimension info.	5
█ Need to determine the symbol for the hitXY	15
█ Maybe put this section to the chapter 4 Yield Estimation	20
█ Todo-Fig: Change A B region in different color	22
█ Present the upper limit at 90% confidence level.	24
█ Fig. compare of photon and neutron-like shape	25

¹ Chapter 1

² Introduction

³ 1.1 Motivation

⁴ massless dark photon has not being search, in theoretic study the branching ratio is up to
⁵ 10^{-3} .

⁶ 1.2 Dark Photon

⁷ **Chapter 2**

⁸ **KOTO Experiment**

⁹ **2.1 Introduction**

¹⁰ The KOTO Experiment is a rare decay experiment. The main goal of this experiment is
¹¹ to search for the $K_L \rightarrow \pi^0 \nu \bar{\nu}$ decay. The branching ratio of this decay is predicted to be
¹² $(3.00 \pm 0.30) \times 10^{-11}$ by the Standard Model (SM) [1]. The branching ratio of this decay
¹³ is sensitive to the new physics beyond the SM because of the accuracy. Therefore, the
¹⁴ KOTO experiment is a good place to search for new physics.

¹⁵ **2.2 $K_L \rightarrow \pi^0 \nu \bar{\nu}$**

¹⁶ **2.3 Beam Line**

¹⁷ The KOTO experiment is located at the J-PARC Hadron Experimental Facility (HEF) in
¹⁸ Tokai, Japan.

¹⁹ The HEF is a 30 GeV proton synchrotron. The proton beam has been generated at
²⁰ the end of a linear particle accelerator (LINAC), then into a 3 GeV rapid cycling syn-
²¹ chrotron (RCS), and finally into a 30 GeV synchrotron (MR). At the end extracted from
²² the synchrotron and directed to the Hadron hall. The proton beam is collided with a gold
²³ target and the secondary particles are then directed to the KOTO detector at a 16° to the
²⁴ beamline.

²⁵ **2.4 Detectors**

²⁶ The KOTO detector consists of an electromagnetic calorimeter and other veto counters
²⁷ in a hermetic veto system. The hermetic veto system encloses the decay volume, which
²⁸ supplies a highly evacuated decay region. The veto system contains barrel vetoes, charge
²⁹ vetoes, and other vetoes.

³⁰ **2.4.1 CsI**

³¹ The electromagnetic calorimeter is the main detector of the KOTO experiment. It is used
³² to detect the photon from the K_L decay. The electromagnetic calorimeter consists of 2716
³³ undoped cesium iodide crystals (CsI). The depth of the CsI is 500 mm. The cross-section
³⁴ of crystals has 2 types of units: the small crystal is 25 × 25 mm with 2240 crystals, and the

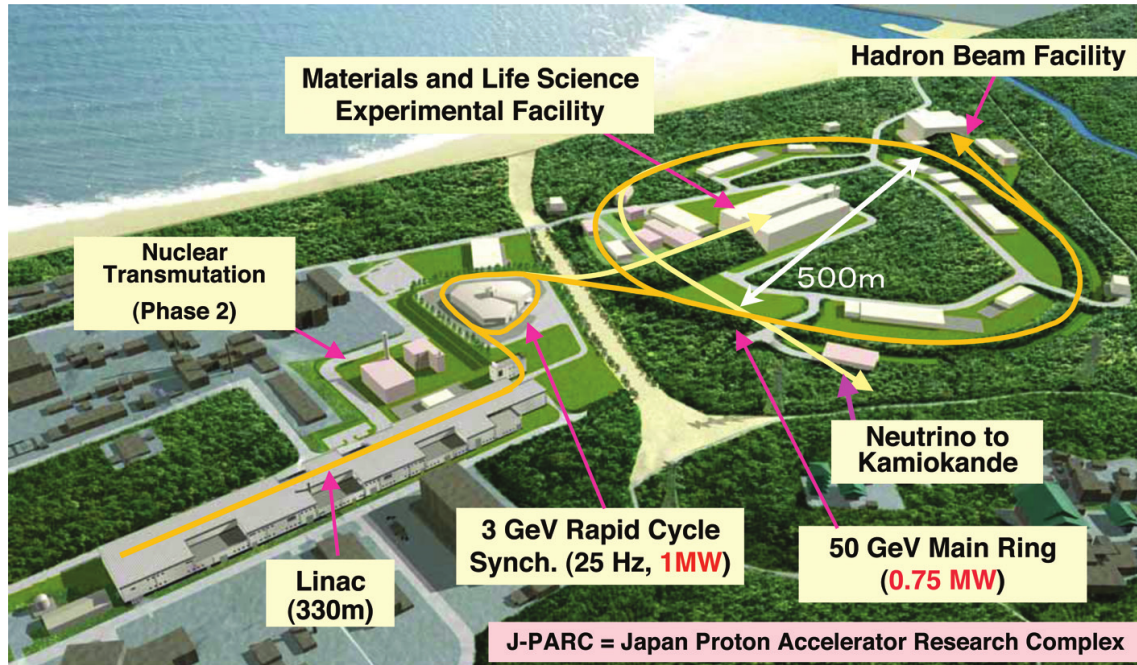


FIGURE 2.1: The entire view of J-PARC. [2]

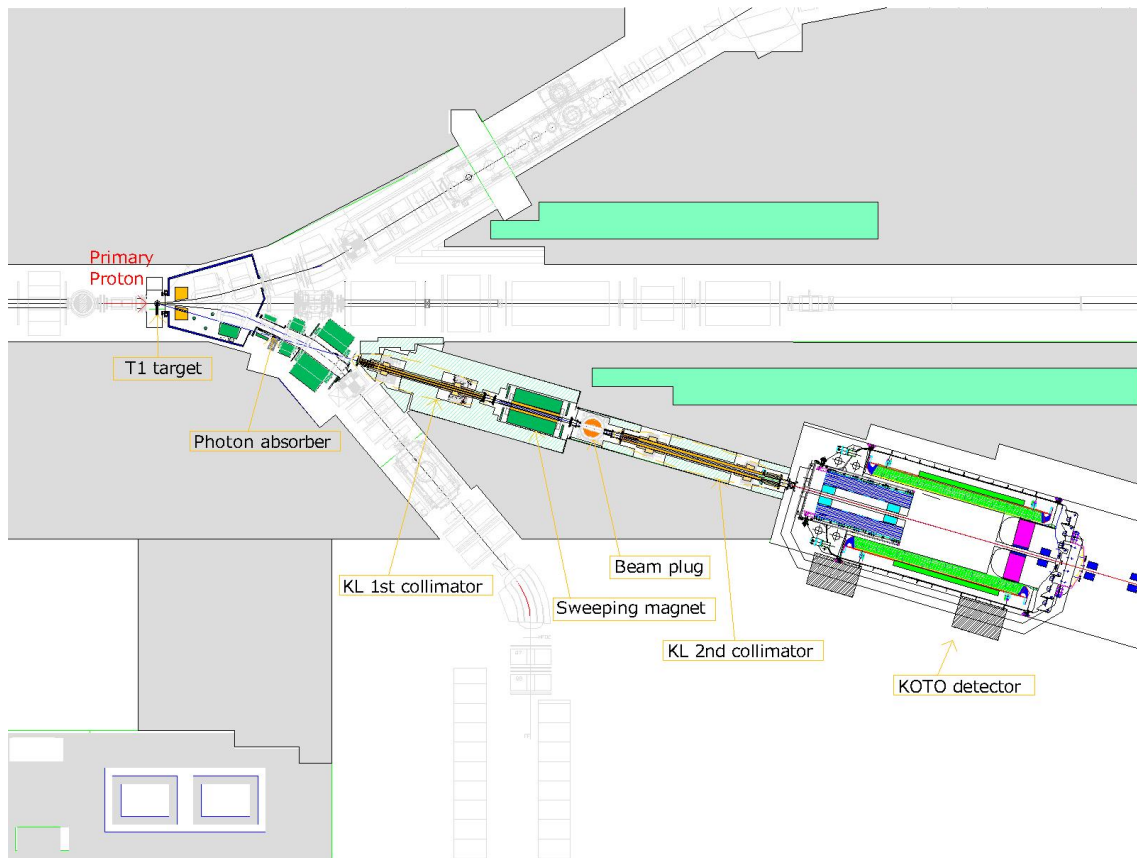


FIGURE 2.2: Beamline layout

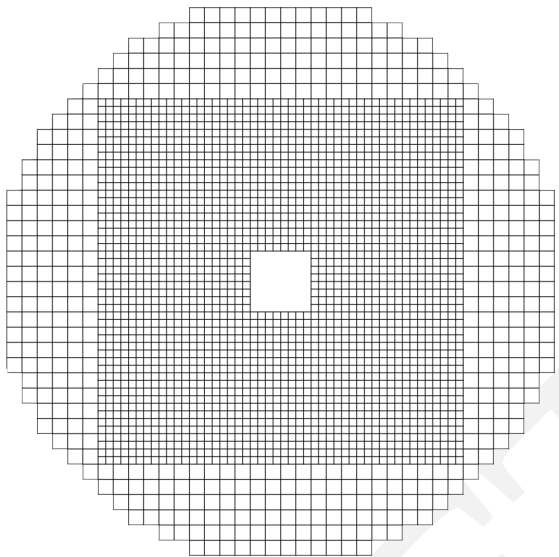


FIGURE 2.3: CsI layout

Add CsI dimension info.

35 large one is 50×50 mm with 476 crystals. The arrangement of those crystals is shown in
36 Figure 2.3. The CsI is used to detect the photon from the K_L decay. The CsI is also used to
37 detect the charged particle from the K_L decay. The CsI is also used to detect the charged
38 particle from the K_L decay. The CsI is also used to detect the charged particle from the
39 K_L decay. The small crystal size is smaller than the Molère radius of 35.7 mm. That
40 allows us to use the shower shape to distinguish the different types of clusters on CsI.
41 When a photon hits the CsI, the EM shower will be induced and the photon multiplier
42 tube (PMT) can observe the deposited energy on each crystal. The PMT is connected to
43 the end of each crystal.

44 In front of the CsI crystal, 4096 Multi-pixel photon counters (MPPC) were glued. This
45 readout system can be used to measure the shower depth in the calorimeter, by evaluat-
46 ing the time difference between both ends of the crystal. Which is potentially useful for
47 discriminating the photon cluster and hadronic-like cluster. Because a hadronic shower
48 is generally deeper than an EM shower cluster.

49 **2.4.2 Barrel Veto**

50 **2.4.3 CV**

51 **2.4.4 Other Veto**

52 **2.5 Data Acquisition System**

53 **2.6 Data Taking**

54 **2.7 Trigger**

55 **2.8 Basic Strategy of the Single Cluster Study**

56 **2.8.1 Signal Identification**

57 $K_L^0 \rightarrow \gamma\bar{\gamma}$ decay requires only one photon cluster to hit the CsI calorimeter and without
 58 any in-time hit in the rest of the detector. A single cluster can only provide the energy
 59 and position information. The lack of kinematic constraints will be the challenge of this
 60 study. Moreover, single cluster signatures are easily mimicked by some unknown arbit-
 61 rary background. Requiring a high photon energy may help to suppress this kind of
 62 background but also reduce the signal efficiency.

63 **2.8.2 Major Background Sources**

64 The major background sources are K_L^0 decay background and neutron-like background.

65 **K_L^0 decay background**

66 Table 2.1 shows the main K_L^0 decay backgrounds. Other decay channels are unneces-
 67 sary to be considered because of the low branching ratio. Only $K_L^0 \rightarrow \pi^\pm e^\mp \nu_e$ and
 68 $K_L^0 \rightarrow \pi^\pm \mu^\mp \nu_\mu$ are considered for the decay channel of charged particles in the final
 69 state, due to the high branching ratio. To suppress the K_L^0 decay background, study-
 70 ing these decay channels and understanding their characteristics are important. All of
 71 these decay channels produce more than one photon in the final state. Therefore, it is
 72 easy to suppress these decay channels with the KOTO detector. Except for the decay of
 73 $K_L^0 \rightarrow 2\gamma$, whose final state is similar to the signal signature and may be a potentially
 74 non-eliminable source of background.

TABLE 2.1: Main K_L^0 decay background modes and their branching ratios.

Decay mode	Branching Ratio
$K_L \rightarrow \pi^\pm e^\mp \nu_e$	$(40.55 \pm 0.11)\%$
$K_L \rightarrow \pi^\pm \mu^\mp \nu_\mu$	$(27.04 \pm 0.07)\%$
$K_L \rightarrow 3\pi^0$	$(19.52 \pm 0.12)\%$
$K_L \rightarrow \pi^+ \pi^- \pi^0$	$(12.54 \pm 0.05)\%$
$K_L \rightarrow 2\pi^0$	$(8.64 \pm 0.06) \times 10^{-4}$
$K_L \rightarrow 2\gamma$	$(5.47 \pm 0.04) \times 10^{-4}$

⁷⁵ **Neutron-like background**

⁷⁶ The neutron originating from the beamline poses a significant background challenge.
⁷⁷ Accurately simulating the in-beam neutron background is nearly impossible, especially
⁷⁸ without a defined mechanism to avoid it. The primary method to mitigate this back-
⁷⁹ ground involves distinguishing the cluster from the photon event.

80 **Chapter 3**

81 **Event Reconstruction**

82 **3.1 Cluster Finding**

83 - CDT

84 **3.2 Veto Hit Reconstruction**

85 - Veto timing - veto hit mechanism – backsplash – fly Backward – upstream decay

86 **3.3 MPPC calibration**

87 **3.3.1 Cosmic Ray analysis**

88 **3.3.2 T0 correction**

89 **3.3.3 $K_L^0 \rightarrow 3\pi^0$ correction**

⁹⁰ **Chapter 4**

⁹¹ **K_L^0 Yield Estimation**

⁹² The flux of K_L is an important parameter for most analysis in KOTO. It could be used in
⁹³ the Monte Carlo normalization and estimate the number of signal events. The K_L flux is
⁹⁴ usually estimated by well-known decays, such as $K_L^0 \rightarrow 3\pi^0$, $K_L^0 \rightarrow \pi^0\pi^0$, and $K_L^0 \rightarrow 2\gamma$.
⁹⁵ The branching ratio of these three decays is shown in the Table 4.1

TABLE 4.1: Branching ratio of K_L decays

Decay mode	Branching ratio
$K_L^0 \rightarrow 3\pi^0$	$(19.52 \pm 0.12)\%$
$K_L^0 \rightarrow \pi^0\pi^0$	$(8.64 \pm 0.06) \times 10^{-4}$
$K_L^0 \rightarrow 2\gamma$	$(5.47 \pm 0.04) \times 10^{-4}$

⁹⁶ The $K_L^0 \rightarrow 3\pi^0$ decay is a good place to estimate the K_L flux because the branching
⁹⁷ ratio is large, and the decay is clean.

⁹⁸ And due to insufficient time for collection of special run data, the statistics of $K_L^0 \rightarrow$
⁹⁹ $\pi^0\pi^0$ decay are not enough to estimate the K_L flux. Therefore, only the $K_L^0 \rightarrow 3\pi^0$ decay
¹⁰⁰ is accepted to estimate the K_L flux.

¹⁰¹ **4.1 Event Selections**

¹⁰² **4.2 Yield Estimation**

¹⁰³ **Chapter 5**

¹⁰⁴ **Monte Carlo Simulation**

¹⁰⁵ **5.1 GEANT4**

¹⁰⁶ **5.2 Accidental Overlay**

¹⁰⁷ **5.3 Beamline simulation**

¹⁰⁸ **5.4 Other Simulations**

¹⁰⁹ **5.4.1 NCC background**

¹¹⁰ **5.4.2 Halo Kaon**

¹¹¹ **5.4.3 Charge Kaon**

¹¹² **Chapter 6**

¹¹³ **Analysis of $K_L \rightarrow \gamma\bar{\gamma}$**

¹¹⁴ The goal of the $K_L^0 \rightarrow \gamma\bar{\gamma}$ analysis is to estimate the branching ratio (\mathcal{BR}) of this decay,
¹¹⁵ we took a 2-hour special run with a single cluster trigger in 2020. The distinctive signal
¹¹⁶ signature of $K_L^0 \rightarrow \gamma\bar{\gamma}$ manifests as a singular photon hit on the CsI calorimeter, devoid
¹¹⁷ of any in-time hits on other detectors.

¹¹⁸ Employing a blind analysis method, we define a specific region, characterized by en-
¹¹⁹ ergy deposition $800 \text{ MeV} < E_\gamma < 3000 \text{ MeV}$ and a spatial constraint of $300 \text{ mm} < R_{XY}$
¹²⁰ $< 850 \text{ mm}$, where R_{XY} denotes the maximum distance between the hit location and the
¹²¹ center of the CsI crystal along the x and y axes. The signal region has to be within the
¹²² blind region and has been optimized.

¹²³ Need to determine the symbol for the hitXY

¹²⁴ Our principal objective revolves around suppressing background noise and accentu-
¹²⁵ ating signal events through event selection. Subsequently, we estimate the residual back-
¹²⁶ ground events within the signal region post-selection. Under the assumption of negli-
¹²⁷ gible background noise, we calculate the Single Event Sensitivity (SES) to estimate the
¹²⁸ branching ratio upon observing signal events within the defined signal region. The SES,
¹²⁹ representing the reciprocal of the product of the total K_L^0 yield and the acceptance of
¹³⁰ signal decays, is expressed mathematically as:

$$SES = \frac{1}{Y \times A_{sig}} \quad (6.1)$$

¹³¹ Here, Y represents the K_L^0 yield, and A_{sig} signifies the signal acceptance. The branching
¹³² ratio (\mathcal{BR}) is then inferred from SES and the observed number of signal events (N_{sig})
¹³³ within the signal region, as articulated by:

$$\mathcal{BR} = SES \times N_{sig} \quad (6.2)$$

¹³⁴ However, when background contributions cannot be negligible, a statistical methodol-
¹³⁵ ogy becomes imperative to ascertain the upper and lower bounds of signal event counts.
¹³⁶ The background level (N_{bg}) is estimated through two approaches in this study. For K_L
¹³⁷ decay backgrounds, Monte Carlo simulations are employed to evaluate N_{bg} , defined by:

$$N_{bg} = Y \times \mathcal{BR}_{bg} \times A_{bg} \quad (6.3)$$

138 Were \mathcal{BR}_{bg} represents the branching ratio of specific background decays (e.g., $K_L \rightarrow 2\gamma$),
 139 and A_{bg} denotes the acceptance corresponding to this background decay. For neutron
 140 backgrounds, a dedicated neutron data run is utilized, employing a data-driven approach
 141 for background-level evaluation through normalization against the neutron-dominant
 142 region between physics data and neutron data sample. Upon combining all background
 143 sources, a prediction of the background level within the signal region is determined. Af-
 144 ter an examination of reliability through the side-band region, uncover the blind region.

145 This chapter unfolds with a presentation of the event selection criteria, followed by
 146 a discussion on background suppression methodologies. Subsequently, the reliability
 147 of our analysis is assessed through a comparison between physics data and simulation
 148 results in the side-band region. The computation of background levels and SES is then
 149 detailed. With the final estimation in hand, we will proceed to open the box and the
 150 interpretation of the statistical result will be presented at the latest.

151 6.1 Event Selection

152 The event selection included trigger cuts, kinematic cuts, and veto cuts. The trigger cuts
 153 were designed to mimic the online trigger effect, while the kinematic cuts and veto cuts
 154 were implemented to suppress background noise. The kinematic cuts were based on the
 155 reconstruction quantities of the photon cluster, while the veto cuts were just the criteria
 156 of hit on the veto counters. In the single cluster study, the signal significance of $K_L \rightarrow \gamma\bar{\gamma}$
 157 is only one photon cluster hit on the CsI calorimeter. And other vetoes keep silent in
 158 time. Which means a very loose condition for hitting events. It is also a challenge for this
 159 study.

160 6.1.1 Trigger Selection

161 The online trigger effect is the source of the difference between the collected data and the
 162 Monte Carlo simulation. To mimic the online trigger effect and ensure the consistency of
 163 the data and MC simulation, two trigger selections were implemented: the trigger timing
 164 cut and the total energy cut.

- 165 • **Timing window**

166 The online trigger will reject all events with any on-time veto hit, thus a trigger
 167 timing window as shown in Figure 6.1 is required to eliminate the online trigger
 168 effect. In the real data taking, due to the 8-ns clock dead time, the real physics data
 169 timing distribution will be wider than the Monte Carlo simulation. A wide enough
 170 timing window is selected to cover the distribution inconsistency between the data
 171 and the MC simulation.

- 172 • **Total Energy**

173 The offline energy cut should be larger than the online ET threshold to eliminate the
 174 online ET trigger effect. The online ET threshold of 300 MeV was required in the

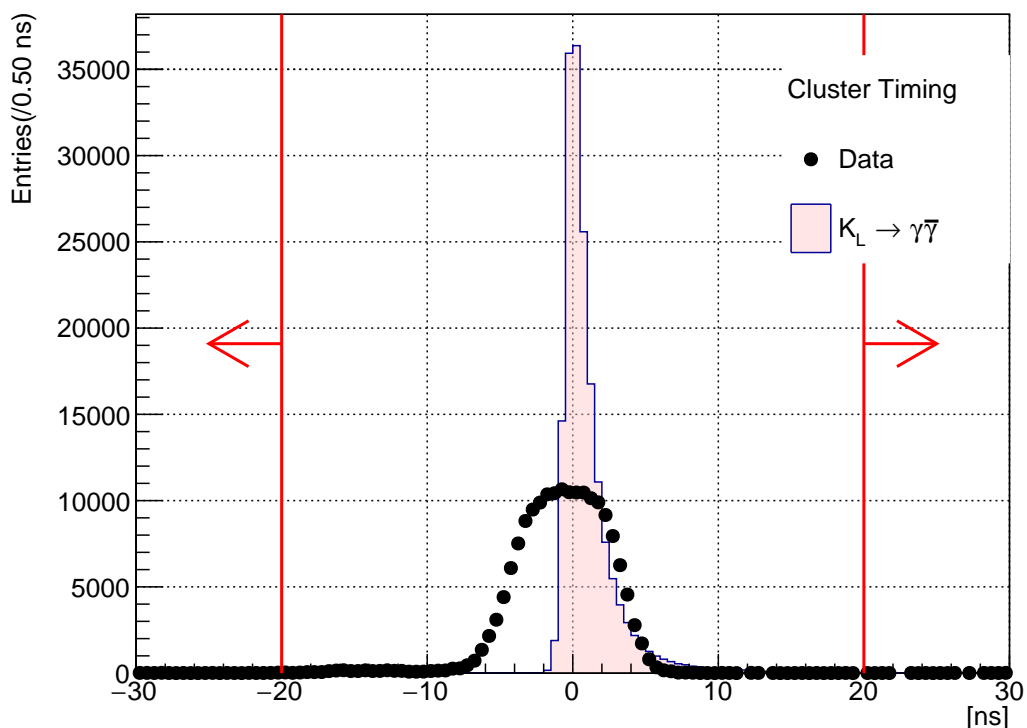


FIGURE 6.1: Distribution of cluster timing after relative timing correction. The dot is from real physics data, and the filled histogram is the MC simulation. The red arrow is the cut-off region.

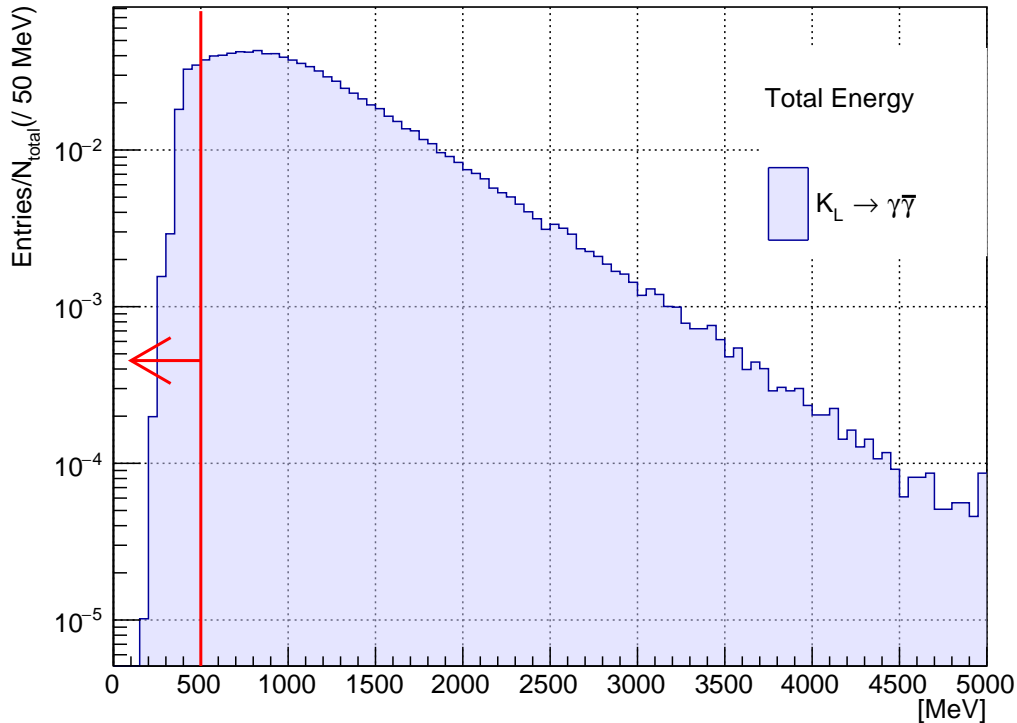


FIGURE 6.2: Distribution of total energy from Monte Carlo simulation. The histogram area is normalized to 1. The red arrow is the cut-off region.

special run, Thus, the offline energy cut is set as 500 MeV. As shown in the Figure 6.2, the signal acceptance is 91.0%

6.1.2 Kinematic Cuts

The $K_L \rightarrow \gamma\bar{\gamma}$ decays require only one photon cluster on the CsI calorimeter. Therefore, the reconstruction of the mother particle is not possible, and also some variables based on multiple photon clusters will be absent, such as the vertex position, cluster distance, and KL kinematic quantities. As kinematic constraints are lacking, kinematic selection is determined by only two variables: the photon hit position and photon energy.

- **Innermost and Outermost Photon Hit Position**

To prevent the edge of the calorimeter from affecting cluster reconstruction, any event that hits the boundary will be removed. Based on the geometry of the calorimeter, the outer boundary is evaluated using radius of hit position, R_γ , while the inner boundary is evaluated using the maximum of the absolute values of x and y of the photon hit position, $\max\{|x_\gamma|, |y_\gamma|\}$. The inner boundary is set as a $300 \times 300 \text{ mm}^2$ box, while the outer boundary is a circle with a radius of 850 mm, as shown in Figure 6.3.

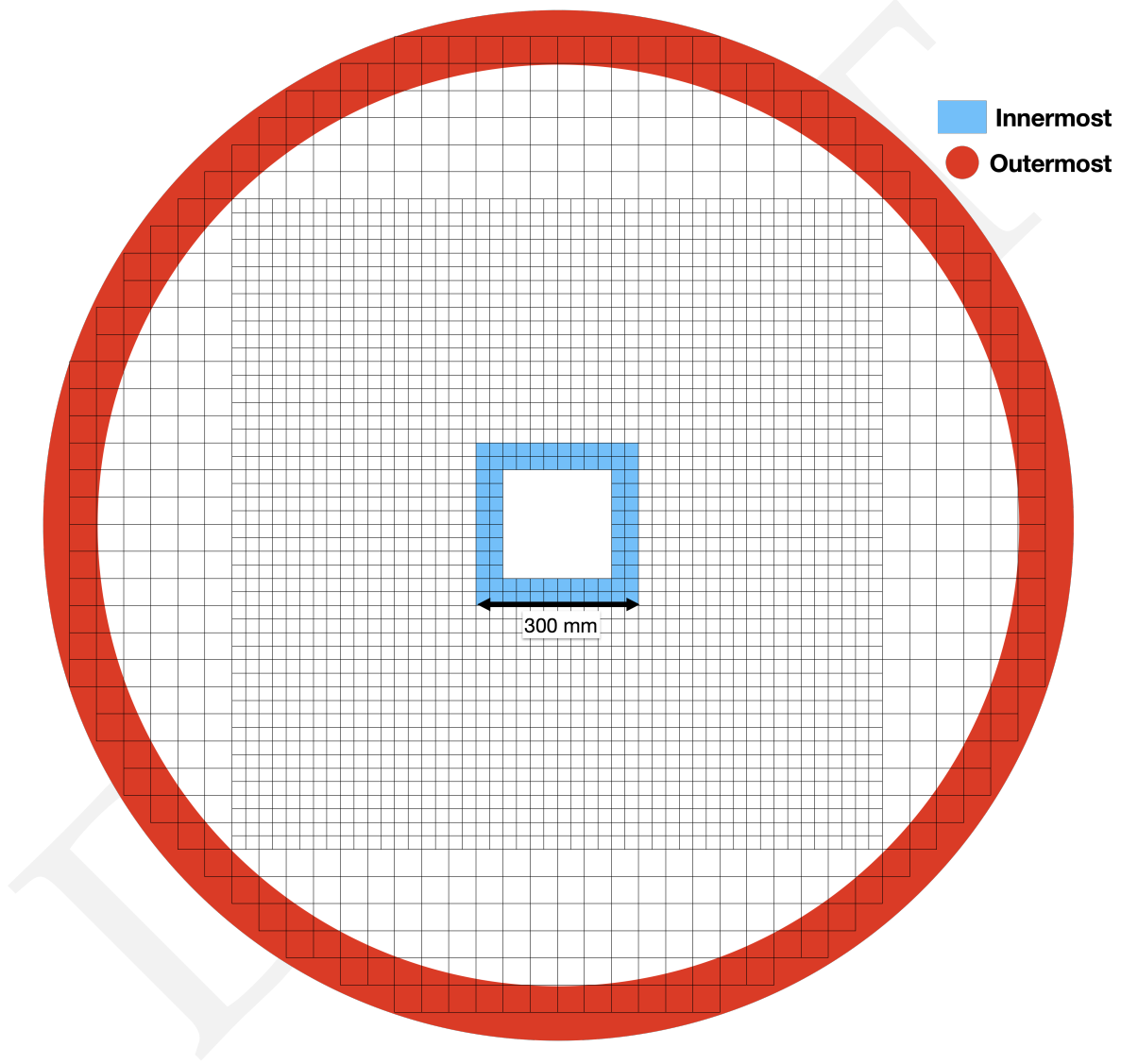


FIGURE 6.3: An upstream view of the CsI calorimeter. The red region is the outermost boundary, while the blue region is the innermost boundary.

191 • **Photon energy**

192 Because of the 1 cluster study, the photon energy is almost equivalent to the total
 193 energy. Therefore, simply required photon energy to be larger than 500 MeV, which
 194 is the same as the total energy cut.

195 **6.1.3 Veto Cuts**

196 Maybe put this section to the chapter 4 Yield Estimation

197 Veto counters are the primary tool for Kaon decay background suppression in the
 198 KOTO experiment. The veto hits within the veto timing window and above the veto
 199 energy threshold will be tagged as an in-time veto hit. The event with any in-time veto
 200 hits will be treated as a background event and rejected. In the following veto cuts study,
 201 the determined method of the veto timing window and the veto energy threshold will be
 202 discussed.

203 **FBAR and NCC**

204 • **Upstream decays**

205 (K_L^0 decays inside the FBAR.)

206 • **Backward hit**

207 (K_L^0 decays inside MB and flies backward to hit FBAR or NCC.)

208 • **CsI backsplash**

209 ()

210 **MB and IB**

211 **CV**

212 **Others**

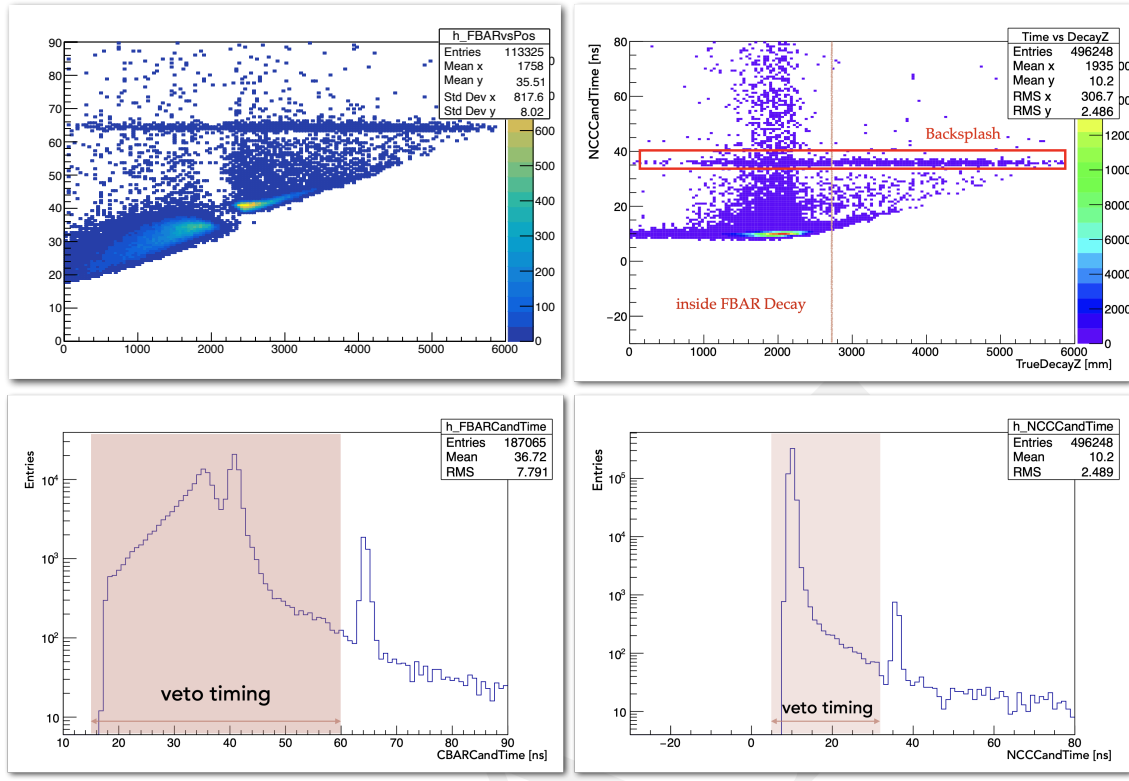
213 (Other Veto counters, CC03, CC04, CC05, CC06, OEV, IBCV, MBCV, BHPV and BHGC.)

214 **6.2 Background Suppression**

215 There are two main category background sources in this analysis: K_L decay events and
 216 Hadronic cluster. Besides these two main background sources, we will also discuss the
 217 other background sources that we study in this analysis, such as Charge Kaon decays,
 218 NCC background, and Halo Kaon backgrounds. In the following section, we will talk
 219 about the background suppression strategy for each category.

220 **6.2.1 K_L Decay Background**

221 In this analysis, we have studied the major three K_L^0 neutral decay channels, like $K_L^0 \rightarrow$
 222 $3\pi^0$, $K_L^0 \rightarrow \pi^0\pi^0$, and $K_L^0 \rightarrow 2\gamma$. And also the K_{e3}^0 , $K_{\mu 3}^0$, and $K_L^0 \rightarrow \pi^+\pi^-\pi^0$, which is the
 223 charge decay channel with a large branching ratio.



(A) fig3

(B) fig4

FIGURE 6.4: Temporary plots of FBAR and NCC

224 There is 3 kinds of possible mechanisms from K_L^0 decays were found:

225 • **Missing photon**

226 One photon hits the CsI, but other particles hit the dead material of the KOTO
227 detector or missing in the beam hole.

228 • **Upstream decay**

229 K_L^0 decay upstream of the FBAR, one photon hits the CsI, and the other photon
230 missing outside the detector.

231 • **Fusion cluster**

232 The decay position along the Z-axis ($Z_{v,tx}$) is too close to the CsI, all decay products
233 hit the nearby crystal and are noted as a single cluster by the clustering process. As
234 shown in Figure 6.7

235 In this section, all the studied K_L^0 backgrounds will be discussed. All the Monte Carlo
236 simulations were applied the accidental overlay.

237 **$K_L^0 \rightarrow 2\gamma$ Background**

238 Because of the extreme hermetic of the KOTO detector, the possibility of missing multiple
239 particles is very low. And with our powerful charge veto counter, it is also very difficult

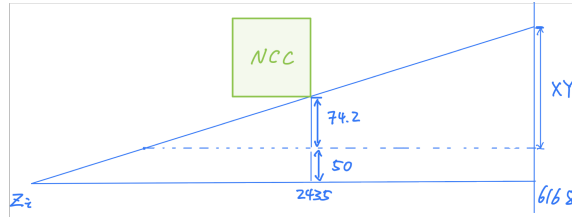


FIGURE 6.5: The schematic geometry diagram of the mechanism of the upstream decay background.

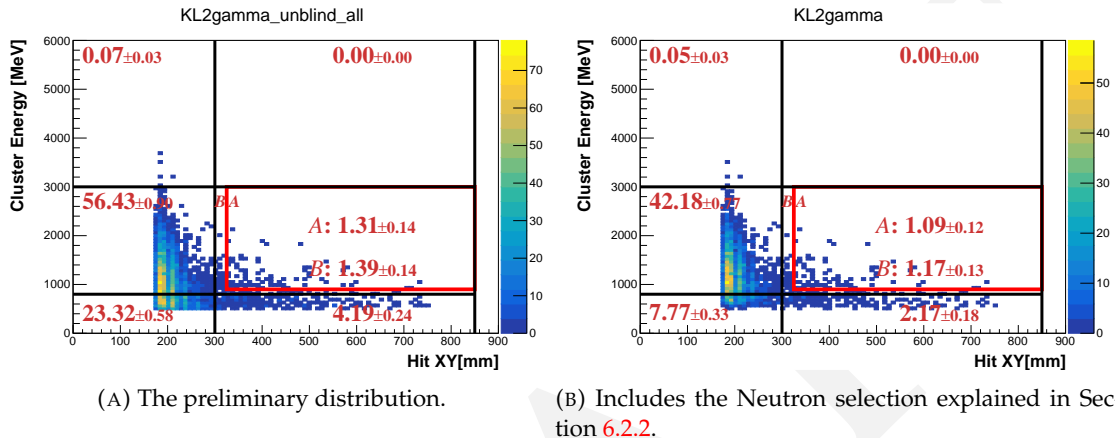


FIGURE 6.6:

Todo-Fig: Change A B region in different color

$E_\gamma - R_{XY}$ distributions of scattered $K_L^0 \rightarrow 2\gamma$ decays with various cut. The red frame indicates the signal region. The red number indicates the background level in each region.

240 to miss a charged particle. Therefore, $K_L^0 \rightarrow 2\gamma$ decay with one missing photon will be
241 the primary K_L^0 decay background in this study.

242 $K_L^0 \rightarrow 2\gamma$ background consists of two mechanisms, missing photon and upstream de-
243 cay. $K_L^0 \rightarrow 2\gamma$ has very similar signature with the $K_L^0 \rightarrow \gamma\bar{\gamma}$, the only difference is another
244 photon is visible. This means if the other photon of $K_L^0 \rightarrow 2\gamma$ is missing detecting, this
245 event will be an ineliminable background in this study. The upstream decay mechanism
246 is also having a missing photon. But its decay position is upstream of the FBAR, which
247 highly constrains the hit radius (R_{XY}) of the cluster. Based on the geometry calculation
248 as shown in Figure 6.5, the maximum R_{XY} of the cluster of upstream decay is 265 mm,
249 which is outside the signal region.

250 Figure 6.6 shows the result of K_L^0 selection. A background level of 1.09 ± 0.12 is esti-
251 mated in the signal region.

252 Other K_L^0 decay Backgrounds

253 Besides the $K_L^0 \rightarrow 2\gamma$ background, the other K_L^0 decay backgrounds are also studied in
254 this analysis. Such as $K_L^0 \rightarrow 3\pi^0$, $K_L^0 \rightarrow \pi^0\pi^0$, K_{e3}^0 , $K_{\mu 3}^0$ and $K_L^0 \rightarrow \pi^+\pi^-\pi^0$. After the

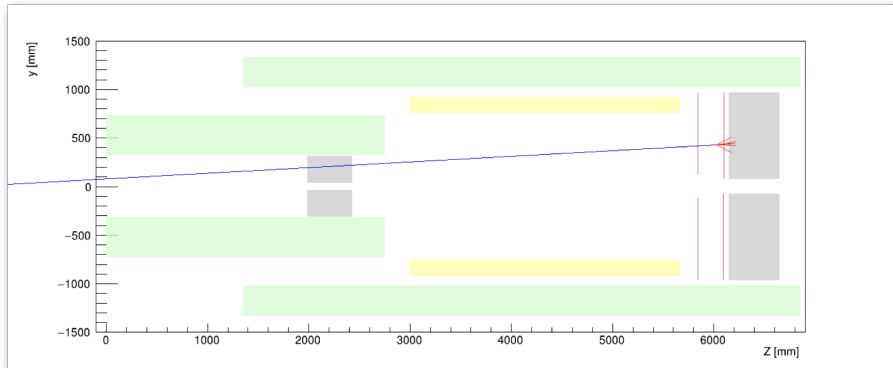


FIGURE 6.7: The schematic geometry diagram of the mechanism of the fusion cluster background.

event selection explained in Section 6.1 and 6.2.2, the event inside the signal region of all decays except $K_L^0 \rightarrow 2\gamma$ is all rejected. All the three mechanisms mentioned above existed in these decays. The missing photon is also an ineliminable background, but because the decay products are much more than the $K_L^0 \rightarrow 2\gamma$, the missing photon background is negligible. And the upstream decay background has the same geometry constraint as the $K_L^0 \rightarrow 2\gamma$.

The fusion cluster mechanism is the most challenging one because the usual method to reject this kind of background is to restrict the decay vertex Z (Z_{vtx}) position in a reasonable region. However, in this study, the Z_{vtx} is not available due to the lack of kinematic variables. Therefore, we have to distinguish the fusion cluster from the single cluster by the cluster shape.

The fusion cluster will have a wider shape than the single cluster because the fusion cluster is the combination of two clusters. Which is more likely to be a hadronic-like cluster. Thus, cluster shape discrimination with deep learning (CSDDL), which is explained in Section 6.2.2, is sensitive to distinguish the fusion cluster from the single cluster.

If we assume the BR to be $\mathcal{O}(10^{-3})$, the number of signal events inside the signal region is $\mathcal{O}(10^5)$. That means the Kaon decay background is negligible in this study.

Figure 6.8 shows the background level of other K_L^0 decays. The upper limit at 90% confidence level is estimated in the signal region, as shown in Table 6.1.

6.2.2 Hadronic Background

Neutron cluster background is the dominant background in this study. The mechanism is that a neutron enters the calorimeter with only one cluster hit, as illustrated in Figure ???. We have three tools to suppress the neutron background: cluster shape discrimination with deep learning (CSDDL), pulse shape discrimination by using Fourier analysis (FPSD), and a shower depth measurement.

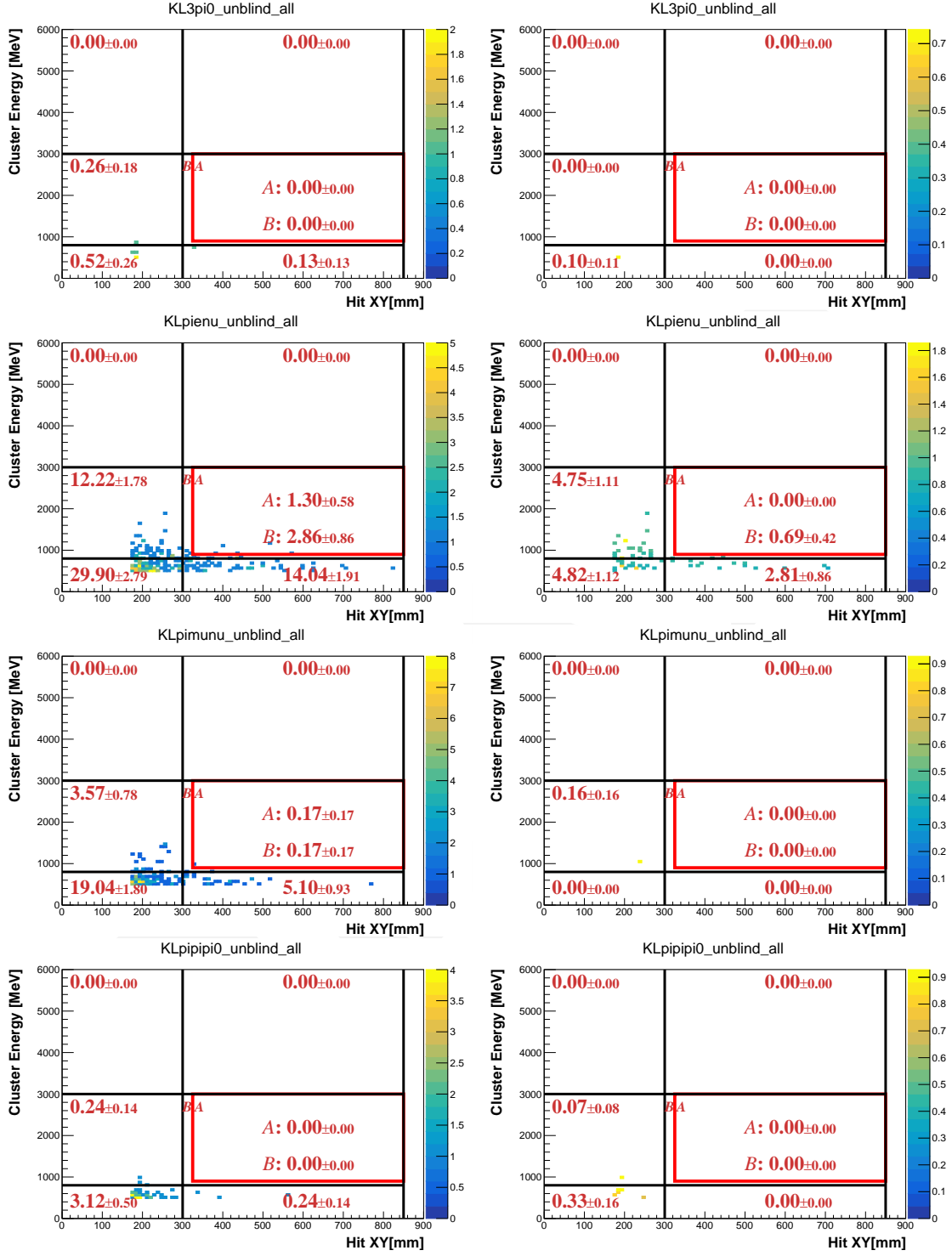


FIGURE 6.8:

Present the upper limit at 90% confidence level.

$E_\gamma - R_{XY}$ distributions of various background sources after applying all selection cuts. Left-hand side plots exclude the neutron cuts and the right-hand side plots include it. The red frame indicates the signal region. The red number indicates the background level in each region.

280 **Cluster Shape Discrimination with Deep Learning(CSDDL)**

281 The cluster shape of hadronic-like events is different from the photon-like events. Be-
 282 cause of the shower depth, the neutron-like event will be wider and shallower, the photon-
 283 like event will look narrow and depth.

284 Fig. compare of photon and neutron-like shape

285 Therefore, we can discriminate each other by cluster shape. However, this discrimina-
 286 tion work is a heavy workload, we use a deep learning model to help us quickly do the
 287 jobs. This model is based on the Convolutional Neural Network (CNN) architecture[3].
 288 The input of the training is the energy and timing of each crystal of the cluster. And the
 289 cluster energy and hit angle (θ).

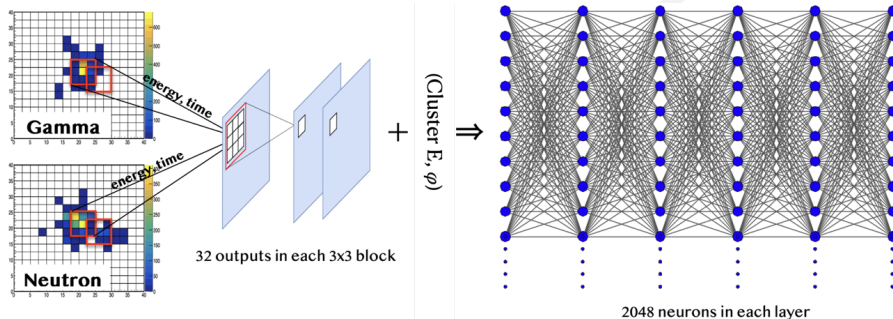


FIGURE 6.9: The architecture of CSD neural network training process.

290 **Fourier transforms for Pulse shape discrimination (FPSD)**

291 The difference in shower development also manifests in the pulse shape difference. FPSD
 292 discriminated the neutron cluster and photon clusters based on the shape of the ADC
 293 waveform. We applied FTT to the ADC raw pulse and then extracted the differences be-
 294 tween the neutron and photon in the frequency domain. Figure 6.10 shows the likelihood
 295 ratio. By requiring the 90% signal acceptance, the neutron cluster background rejection
 296 efficiency is 89.6%.

297 **Shower-depth**

298 The radiation length for photons is shorter than the interaction length for neutrons, re-
 299 sulting in different shower depths in the calorimeter for photons and neutrons. Multi-
 300 pixel photon counters (MPPC) were installed in front of the CSI calorimeter, to get the
 301 timing difference(ΔT) between PMT and MPPC as shown in figure 6.11. The distribution
 302 of ΔT is shown in figure 6.12. By requiring ΔT to be less than 29.5 ns, the background
 303 rejection efficiency is 84% with a signal loss of 9%.

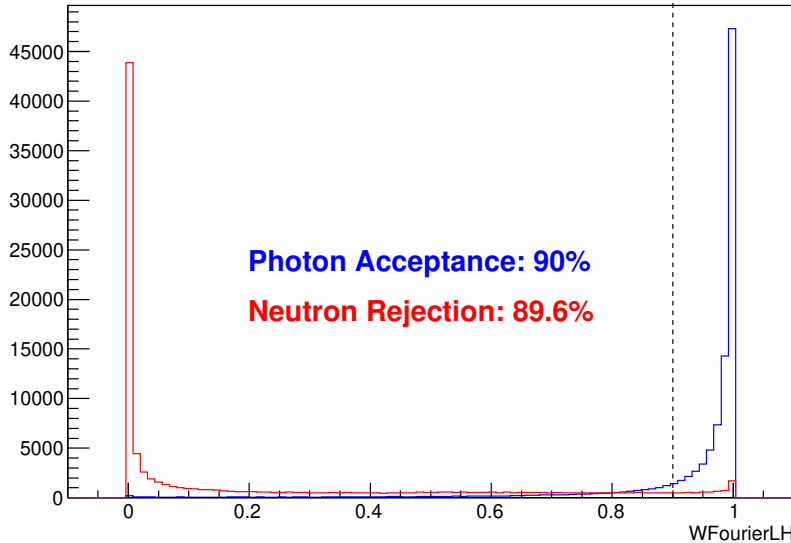


FIGURE 6.10: Distribution of the likelihood ratio for hadronic cluster events (red) and photon cluster events (blue). The photon cluster events are obtained through the $K_L^0 \rightarrow 3\pi^0$ decay analysis of data. The neutron sample is obtained from neutron data.

304 6.2.3 Low Radius Event background

305 After the event selection, there is a large discrepancy between the data and the simula-
 306 tion in the low-radius region. As shown in Figure 6.13, the data has a higher level of
 307 background in the low-radius region than the simulation. To figure out the contribution
 308 of this discrepancy, we studied the following background sources.

309 Upstream Decay from 2nd Collimator

310 The discrepancy is centered at the region $R_{XY} < 175$ mm and the maximum R_{XY} of the
 311 cluster of upstream decay is 265 mm, as Section 6.2.1 discussed. This means the upstream
 312 decay is a very possible background source. Therefore, we extend the generated position
 313 in the Monte Carlo simulation to the start of the 2nd collimator to study the very up-
 314 stream decay background. In the usual simulation, the decay position is generated at
 315 the end of the 2nd collimator, which is -1507 mm from the upstream of the FBAR. The
 316 2nd collimator is 4 m long, which means the new decay position is -5507 mm from the
 317 upstream of the FBAR. The geometry calculation, as Figure 6.5, shows that the maximum
 318 R_{XY} of the cluster of the new decay position is 133 mm, which completely covers the
 319 discrepancy region.

320 The $K_L^0 \rightarrow 2\gamma$ decay was studied in this section. The normalization method is the
 321 same as the usual Monte Carlo simulation but uses the upstream $K_L^0 \rightarrow 3\pi^0$ decay ($Z=-$
 322 5507mm) to estimate the K_L^0 yield.

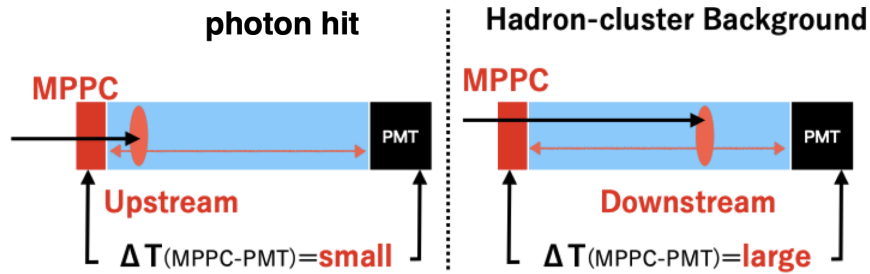


FIGURE 6.11: Illustration of shower depth means. An MPPC is installed on the upstream side. The time difference between the photon arriving upstream and downstream ($\Delta T = T_{MPPC} - T_{PMT}$) is used to measure the depth of the reaction and distinguish between photon events (left) and neutron events (right).

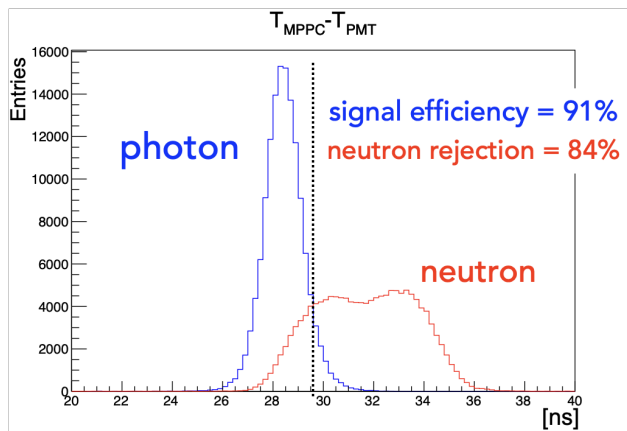


FIGURE 6.12: Distribution of the ΔT for neutron events and photon events. The photon cluster events are obtained through the $K_L^0 \rightarrow 3\pi^0$ decay analysis of data. The neutron sample is obtained by scattering neutrons in the beam with an Al plate.

323 Upstream π^0 background

324 Charge Kaon Decay

325 Halo Kaon Background

326 6.3 Single Event Sensitivity

327 6.4 Background Level Estimation

328 Table 6.1 shows the background level of each background source in the signal region. The
329 upper limit at 90% confidence level is estimated in the signal region.

330 6.5 Unblind and Results

331 6.6 Massive Dark Photon Search

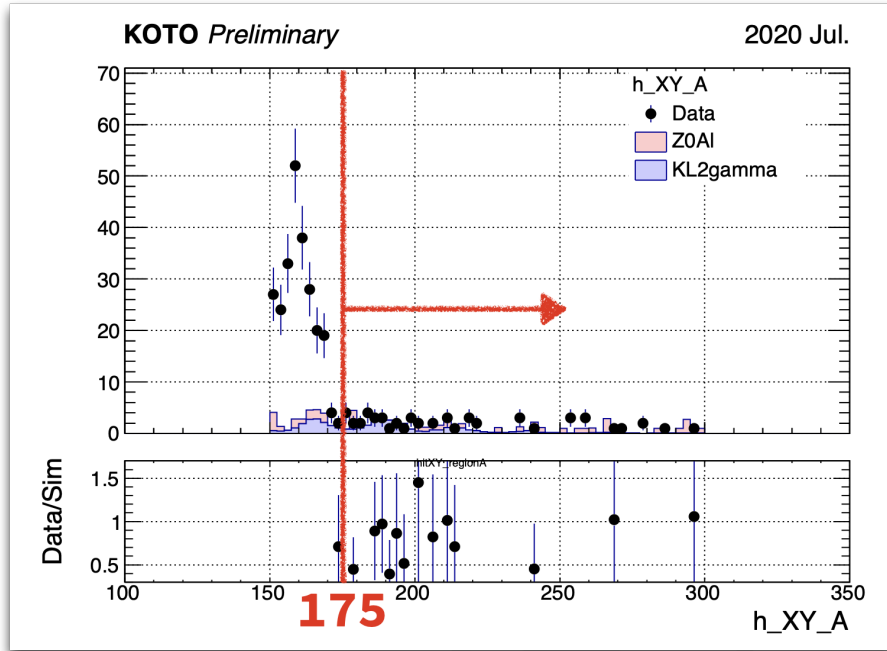


FIGURE 6.13: The R_{XY} distribution of the region 2. The red line and arrow indicated the cutoff region

TABLE 6.1: Number of events predicted for each source inside the signal region

Source		Number of events
K_L decay	$K_L \rightarrow 2\gamma$	1.09 ± 0.12
	$K_L \rightarrow 3\pi^0$	< 0.18 (90% C.L.)
	$K_L \rightarrow 2\pi^0$	< 0.51 (90% C.L.)
	$K_L \rightarrow \pi^\pm e^\mp \nu_e$	< 0.27 (90% C.L.)
	$K_L \rightarrow \pi^\pm \mu^\mp \nu_\mu$	< 0.25 (90% C.L.)
	$K_L \rightarrow \pi^+ \pi^- \pi^0$	< 0.17 (90% C.L.)
Neutron		11.57 ± 4.42

³³² Chapter 7

³³³ Conclusion and Discussion

³³⁴ 7.1 blah

³³⁵ blah blah blah

³³⁶ Bibliography

- ³³⁷ [1] Andrzej J. Buras et al. “ $K^+ \rightarrow \pi^+ \nu \bar{\nu}$ and $K_L \rightarrow \pi^0 \nu \bar{\nu}$ in the Standard Model: status
³³⁸ and perspectives”. In: *Journal of High Energy Physics* 2015.11 (Nov. 2015). DOI: [10.1007/jhep11\(2015\)033](https://doi.org/10.1007/jhep11(2015)033).
- ³⁴⁰ [2] Shoji Nagamiya. “Introduction to J-PARC”. In: *Progress of Theoretical and Experimental
341 Physics* 2012.1 (Oct. 2012). 02B001. ISSN: 2050-3911. DOI: [10.1093/ptep/pts025](https://doi.org/10.1093/ptep/pts025).
- ³⁴² [3] Y. -C. Tung et al. “Suppression of neutron background using deep neural network
343 and Fourier frequency analysis at the KOTO experiment”. In: *Nucl. Instrum. Meth. A*
344 1059 (2024), p. 169010. DOI: [10.1016/j.nima.2023.169010](https://doi.org/10.1016/j.nima.2023.169010).